bubble, compared to the inner 0.03 μm of the N_2 bubble. The radiating volume of Ar is ≈220 times greater than that of N_2, and so, despite the opacity differences, the Ar bubble is brighter. This analysis may explain why SBSL is brighter in noble gases than in diatomic gases (8). We believe that these results provide strong support for the hypothesis of Lohse *et al.* (10) that a sonoluminescing air bubble contains mostly Ar.

The calculated spectra and power are sensitive to small changes in the expansion ratio, which also correspond to moderate changes in the amplitude of the driving pressure near the bubble. The short dashed lines in Figs. 2 and 3 show the calculated results for an Ar bubble with R_{max}/R_0 = 10.4. The two expansion ratios represent only a 0.006-bar difference in the driving pressure at the flask, which equals a 0.07-bar difference in the driving pressure near the bubble (22). Although the $R(t)$ values are similar, the pulse width (24 ps versus 43 ps), the peak amplitude of the emitted power (14 mW versus 32 mW), the number of photons per flash (0.6 million versus 1.9 million), and the spectra are sensitive to R_{max}/R_0 (the driving pressure). Experimental data exhibit this same sensitivity (26). This result suggests that the reported sensitivities of SBSL to various parameters may be difficult to analyze quantitatively without concomitant measurements of R_0 and R_{max}/R_0 for each experiment.

The photon emission rate for the R_{max}/R_0 = 10.0 Ar calculation has a peak value of 2×10^4 ps^{-1} at t = 103 ps and a value of 10 ps^{-1} at t = 200 ps. It has been speculated that, after the "flash," there still should be visible radiation from the hot bubble as it expands and cools. Our model predicts that this afterglow will not occur, in agreement with experimental data (11). Equation 3 shows that an optically thin plasma cannot radiate if its opacity is low, even if its temperature is high. When the temperature in the bubble drops below IP/4, the opacity in our model drops precipitously, which terminates the flash and all subsequent optical emission. Consequently, there is no afterglow as the bubble expands and cools. Our calculations show that the short pulse width and lack of afterglow are intimately related and are due to electron conduction, adiabatic cooling behind the divergent shock, and the strong temperature dependence of the opacity.

The physics of matter under SL conditions is not yet understood with high precision. Our results, based on approximate thermodynamic and transport property models, suggest that the basic strategy of hydrodynamic code simulation is valid and that semiquantitative predictions are possible. Although it remains to be confirmed experimentally that shock waves or plasmas are present in a bubble undergoing SL, no other model of which we are aware has been able to explain such a broad array of experimental data.

REFERENCES AND NOTES

1. D. F. Gaitan, thesis, University of Mississippi (1990).
2. D. F. Gaitan *et al.*, *J. Acoust. Soc. Am.* **91**, 3166 (1992).
3. B. P. Barber and S. J. Putterman, *Nature* **352**, 318 (1991).
4. R. Hiller, S. J. Putterman, B. P. Barber, *Phys. Rev. Lett.* **69**, 1182 (1992).
5. C. C. Wu and P. H. Roberts, *ibid.* **70**, 3424 (1993).
6. W. C. Moss, D. B. Clarke, J. W. White, D. A. Young, *Phys. Fluids A* **6**, 2979 (1994).
7. T. J. Matula *et al.*, in preparation.
8. R. Hiller, K. Weninger, S. J. Putterman, B. P. Barber, *Science* **266**, 248 (1994).
9. Ya. B. Zel'dovich and Yu. P. Raizer, *Physics of Shock Waves and High-Temperature Hydrodynamic Phenomena* (Academic Press, New York, 1966), chaps. I–III.
10. D. Lohse *et al.*, *Phys. Rev. Lett.* **78**, 1359 (1997).
11. T. J. Matula, unpublished data. No afterglow could be observed, even after gating out the main flash, to within the limits of the resolution of the equipment.
12. Ya. B. Zel'dovich and Yu. P. Raizer, *Physics of Shock Waves and High-Temperature Hydronamic Phenomena* (Academic Press, New York, 1966), chaps. VI–VII.
13. $T_i \neq T_e$ would be very important if we considered the possibilities for microthermonuclear fusion in a sonoluminescing D_2 bubble, which requires ion temperatures exceeding 200 eV [W. C. Moss, D. B. Clarke, J. W. White, D. A. Young, *Phys. Lett. A* **211**, 69 (1996)].
14. C. A. Iglesias and F. J. Rogers, personal communication.
15. G. C. Pomraning, *The Equations of Radiation Hydrodynamics* (Pergamon, New York, 1973), pp. 44–49.
16. R. Löfstedt *et al.*, *Phys. Fluids A* **5**, 2911 (1994) (figure 1).
17. G. B. Zimmerman, *Lawrence Livermore Natl. Lab. Rep. UCRL-74811* (1973).
18. J. von Neumann and R. D. Richtmyer, *J. Appl. Phys.* **21**, 232 (1950).
19. J. W. White, *J. Comp. Phys.* **12**, 553 (1973).
20. D. A. Young, unpublished results.
21. ——— and E. M. Corey, *J. Appl. Phys.* **78**, 3748 (1995).
22. W. C. Moss, *J. Acoust. Soc. Am.* **101**, 1187 (1997).
23. F. J. Rogers, *Phys. Rev. A* **24**, 1531 (1981).
24. Ya. B. Zel'dovich and Yu. P. Raizer, *Physics of Shock Waves and High-Temperature Hydrodynamic Phenomena* (Academic Press, New York, 1966), chap. V.
25. W. H. Lokke and W. Grasberger, *Lawrence Livermore Natl. Lab. Rep. UCRL-52276* (1977).
26. See (8), figure 4; B. P. Barber *et al.*, *Phys. Rev. Lett.* **74**, 5276 (1995) (figure 2); B. P. Barber *et al.*, *ibid.* **72**, 1380 (1994) (figure 2).

27. We thank the B-Div. and the LASNEX code groups for technical and computational support. Computational support from J. Levatin, and technical critiques by J. White, T. Ladd, T. Gay, and especially T. Matula, are appreciated greatly. Funding was provided by N. Burkhard through the Lawrence Livermore National Laboratory (LLNL) Containment Program. This work was performed under the auspices of the U.S. Department of Energy by LLNL under contract W-7405-Eng-48.

7 February 1997; accepted 1 April 1997

Block Copolymer Lithography: Periodic Arrays of ~10^{11} Holes in 1 Square Centimeter

Miri Park, Christopher Harrison, Paul M. Chaikin, Richard A. Register, Douglas H. Adamson

Dense periodic arrays of holes and dots have been fabricated in a silicon nitride–coated silicon wafer. The holes are 20 nanometers across, 40 nanometers apart, and hexagonally ordered with a polygrain structure that has an average grain size of 10 by 10. Spin-coated diblock copolymer thin films with well-ordered spherical or cylindrical microdomains were used as the templates. The microdomain patterns were transferred directly to the underlying silicon nitride layer by two complementary techniques that resulted in opposite tones of the patterns. This process opens a route for nanometer-scale surface patterning by means of spontaneous self-assembly in synthetic materials on length scales that are difficult to obtain by standard semiconductor lithography techniques.

In general, feature sizes greater than 300 nm are routinely produced by photolithography techniques. For feature sizes between 300 and 30 nm, electron beam lithography is commonly used. However, feature sizes less than 30 nm are not easily obtained by standard semiconductor lithography techniques. Because of the drive toward smaller, faster, and denser microelectronic systems, different novel techniques for nanolithography have been investigated by many researchers (1). Self-assembly in synthetic materials as a means of nanopatterning has also been proposed recently (2). Electronic circuits often require complex multilevel lithography, but in many devices, simple periodic patterning is sufficient. Various applications of nanometer periodic patterning would include the creation of a periodic

M. Park, C. Harrison, P. M. Chaikin, Department of Physics, Princeton University, Jadwin Hall, Princeton, NJ 08544, USA.
R. A. Register, Department of Chemical Engineering, Princeton University, Princeton, NJ 08544, USA.
D. H. Adamson, Princeton Materials Institute, Princeton University, Princeton, NJ 08544, USA.

electric potential in a two-dimensional (2D) electron gas system (*3*, *4*), fabrication of quantum dots or antidots (*4*, *5*), synthesis of DNA electrophoresis media (*6*), fabrication of high-density magnetic recording devices (*7*) or of filters with nanometer pore sizes, and creation of quantum confinements for light emission. For these applications, ordered diblock copolymers would seem ideal as lithography templates (*8*–*11*). Here we present a successful route for the transfer of dense periodic patterns, over a large area, from diblock copolymer thin films into silicon nitride with feature sizes less than 30 nm.

Diblock copolymers consist of two chemically different polymer chains (or blocks) joined by a covalent bond. Because of connectivity constraints and the incompatibility between the two blocks, diblock copolymers spontaneously self-assemble into microphase-separated nanometer-sized domains that exhibit ordered morphologies at equilibrium (*12*). In a given diblock copolymer system, the relative chain lengths of the blocks determine the resulting morphology. Commonly observed microdomain morphologies in bulk samples are periodic arrangements of lamellae, cylinders, and spheres. The sizes and periods of these microdomain structures are governed by the chain dimensions and are typically on the order of 10 nm. Structures smaller than 10 nm are also obtainable if one chooses appropriate blocks with a high Flory-Huggins interaction parameter (*12*) and decreases the block lengths. Diblock copolymer thin films spontaneously form nanometer-scale patterns over a large area. Furthermore, each block of the copolymer can be chosen for a specific application, and selective processing of one block relative to the other is possible by use of chemical or physical dissimilarities between the two blocks. We used a monolayer of ordered microdomains to fabricate positive and negative patterns with a periodicity less than 40 nm. A similar periodic patterning by electron beam lithography would be limited in three aspects. First, routine production of patterns with feature sizes below 30 nm is difficult to achieve with commercial electron beam systems, and, at best, the minimum feature size is ~10 to 15 nm. Second, the obtainable minimum periodicity of features is still not much below 100 nm (at best, ~50 nm). Third, as with any scanning probe techniques, large-area lithography would be time-consuming because the processing is serial.

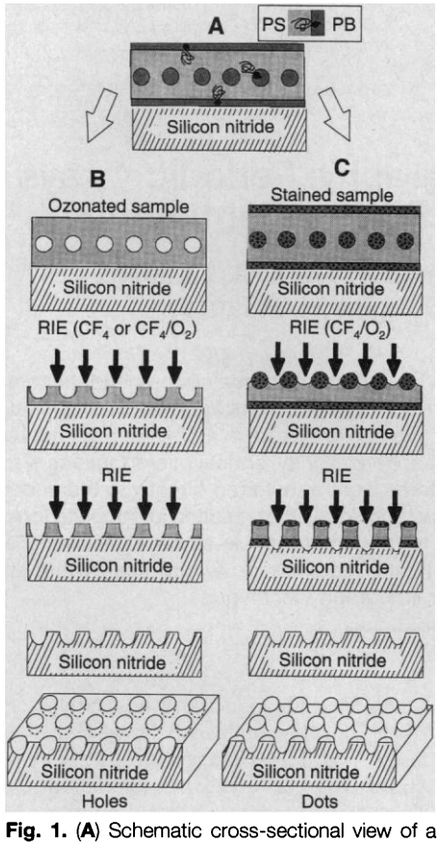

Fig. 1. (**A**) Schematic cross-sectional view of a nanolithography template consisting of a uniform monolayer of PB spherical microdomains on silicon nitride. PB wets the air and substrate interfaces. (**B**) Schematic of the processing flow when an ozonated copolymer film is used, which produces holes in silicon nitride. (**C**) Schematic of the processing flow when an osmium-stained copolymer film is used, which produces dots in silicon nitride.

Asymmetric polystyrene-polybutadiene (PS-PB) and PS-polyisoprene (PI) diblock copolymers were synthesized (designated SB 36/11 and SI 68/12, respectively, with the approximate molecular weights of the blocks given in kilograms per mole). In bulk, the SB 36/11 microphase separates into a cylindrical morphology and produces hexagonally ordered PB cylinders embedded in a PS matrix; SI 68/12 adopts a spherical morphology and produces PI spheres in a PS matrix with body-centered-cubic order. We produced thin polymer films by spin-coating polymer solutions in toluene onto silicon nitride (*13*) and controlled the film thickness by varying spinning speed and polymer concentration. The films were annealed at 125°C, a temperature above their glass transition temperatures, for 24 hours in vacuum to obtain well-ordered morphologies.

Our nanolithography template is a monolayer of ordered microdomains. To pattern the whole substrate, a uniform microdomain monolayer must be produced over the substrate area in a controlled manner. Such a microdomain monolayer on silicon nitride, depicting the continuous PB wetting layers at the air and silicon nitride interfaces for a PS-PB diblock copolymer film, is shown (Fig. 1A). [The existence of such wetting layers is confirmed by secondary ion mass spectroscopy (*14*).] For the SB 36/11 film on silicon nitride, the microdomain monolayer thickness is ~50 nm, including the wetting layers (*14*). By spin-coating at this thickness, a uniform template can be routinely obtained over the entire sample area (*15*).

We show schematically how to fabricate hexagonal arrays of holes and dots in silicon nitride from a spherical microdomain monolayer that consists of PB spheres ordered in a 2D hexagonal lattice (*10*) (Fig. 1). We used fluorine-based reactive ion etching (RIE) techniques (*16*) to transfer the microdomain pattern in the monolayer to the underlying silicon nitride, with the copolymer film itself as the etching mask. The unaltered microphase-separated PS-PB film alone does not produce a usable RIE mask because the etching rates of the PS and PB microdomains are almost the same under most RIE conditions. To transfer the pattern, a selective etching or masking between dissimilar microdomain regions is essential. The microdomain monolayer film was exposed to ozone to selectively degrade and remove the PB spherical domains before a CF_4RIE or CF_4/O_2 RIE (*17*) (Fig. 1B). Ozone predominantly attacks the carbon-carbon double bonds in the PB backbone, cutting the bonds and producing PB fragments that can be dispersed in water. This results in regular spherical voids in the PS matrix and hence in a variation of the effective total thickness of the copolymer mask. The regions underneath the empty spheres are protected by a thinner PS mask than is the rest of the area and therefore can be exposed to the RIE, whereas the rest is still protected to produce holes in silicon nitride. A transmission electron microscope (TEM) image (*18*) of a PB spherical microdomain monolayer (*19*) after ozonation, where the empty spheres appear lighter than the PS matrix, is shown (Fig. 2A). A TEM micrograph of hexagonal arrays of holes fabricated in silicon nitride from a copolymer film such as that in Fig. 2A is also shown (Fig. 2B). The remaining polymer has been completely removed, and the contrast in Fig. 2B is due to a thickness modulation. The holes [~15 nm deep (*20*)] appear lighter, and their period is 30 nm, resulting in a density of 1.3×10^{11} holes per square centimeter.

The second processing technique, which results in the fabrication of dots instead of holes in silicon nitride and uses the same spherical microdomain monolayer template, is schematically described (Fig. 1C). In this technique, CF_4/O_2 RIE (*17*) is used and etching selectivity is achieved by stain-

ing the PB domains with osmium. Exposing the copolymer films to OsO_4 vapor results in a selective staining of PB because osmium adds across the carbon-carbon double bonds in the PB backbone. Osmium staining reduces the etching rate of the PB domains during the CF_4/O_2 RIE (*21*), producing an etching selectivity of PS to stained PB of ~2:1. The regions underneath the PB domains are thus partially masked from the RIE process, resulting in the fabrication of dots. The electron beam exposure done on the sample during the examination of the monolayer template before the etching process appears to enhance the contrast of the transferred microstructures.

The schematics shown in Fig. 1 are drawn with a spherical microdomain monolayer as the template. However, the pattern transfer techniques can also be applied to produce lines, with the use of a monolayer of cylindrical microdomains as the template. In thin films, cylindrical microdomains generally lie parallel to the substrate and form a fingerprintlike pattern; with such a template, fingerprintlike troughs [in the case of an ozonated sample (Fig. 1B)] or lines [in the case of a stained sample (Fig. 1C)] can be fabricated. A TEM micrograph of a cylindrical microdomain monolayer, consisting of osmium-stained PB cylinders in a PS matrix, is shown (Fig. 2C). The stained PB cylinders appear darker than the PS domains because of greater high-angle electron scattering. A TEM micrograph of the pattern in silicon nitride that was transferred from a stained copolymer film such as that in Fig. 2C is shown (Fig. 2D). The remaining polymer was removed, and the contrast in Fig. 2D was produced by a thickness modulation. The darker regions are thicker [~15 nm (*20*)] silicon nitride lines that were protected by the stained PB microdomains; the period of the lines is 30 nm.

To show the utility of our techniques for more practical lithographic processes, we used a spherical-phase copolymer, spin-coated and processed the polymer films on a thick wafer, and made all observations with a scanning electron microscope (SEM). A uniform monolayer film of spherical microdomains was obtained from SI 68/12, a spherical PS-PI block copolymer. With this copolymer, the thickness of a microdomain monolayer was ~70 nm (*22*), and a uniform template of ordered PI spheres was routinely produced over an entire 76-mm wafer. The 2D microdomain morphology in the copolymer template on a thick substrate was directly imaged by an SEM technique combined with a nonselective RIE. This technique (*23*) allows one to depth profile copolymer films with ~10-nm depth resolution. For the film-processing steps discussed in this report, PI blocks behave similarly to PB blocks. The PI blocks also wet the air and silicon nitride interfaces (see Fig. 1A), and any selective processing performed on PS-PB copolymer films can also be performed on PS-PI copolymer films. An SEM micrograph of periodic arrays of holes in a silicon nitride–covered silicon wafer is shown (Fig. 3B). The pattern was transferred to the silicon nitride layer from an ozonated SI spherical monolayer film (see Fig. 1B). An SEM micrograph of the copolymer mask partially etched so that the ozonated empty spheres are exposed is also shown (Fig. 3A). In an SEM micrograph, the holes [~20 nm deep (*20*) in Fig. 3, A and B] appear darker because fewer secondary electrons can escape from the depressions. The typical size of the arrays is ~10 by 10. The period of the holes is 40 nm, which results in a density of 7×10^{10} holes per square centimeter. We have fabricated structures such as that shown in Fig. 3 uniformly over an area as large as a quarter of a 76-mm silicon wafer, putting 8×10^{11} holes in that quarter of a wafer by a single process. [The sample size is not the limitation of this technique. One quarter of a wafer is the largest piece that can fit in our ozonator (*24*).]

Successful pattern transfer to silicon nitride was possible because the etching rate of silicon nitride is at least comparable to or slightly faster than PS under the RIE conditions used above, resulting in the fabrication of nanostructures with an aspect ratio of ~1. If the etching rate of the substrate is negligible under a given RIE condition, then even if selective etching is possible between the two blocks, no pattern can be transferred to the substrate unless multiple RIE steps are taken with different gases. However, if the etching rate of the substrate is increased relative to the rate of the polymer mask, then fabrication of features with higher aspect ratios would be possible.

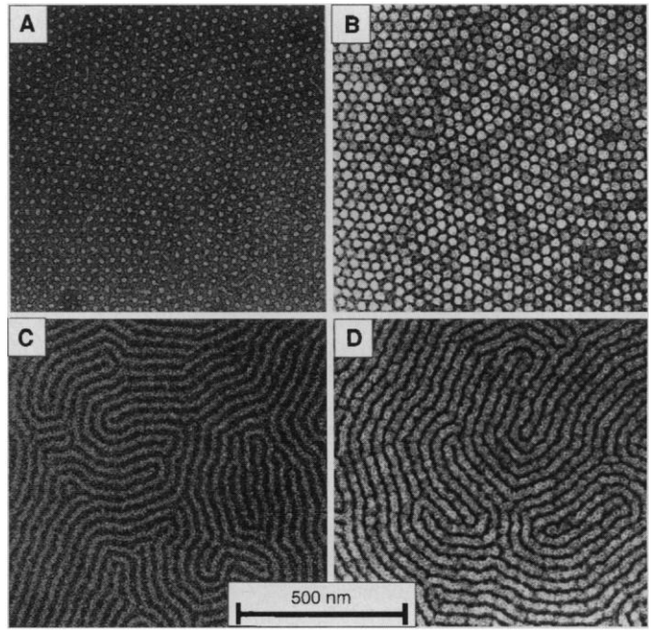

Fig. 2. A series of TEM micrographs showing film processing. (**A**) A spherical microdomain monolayer film before RIE. The lighter regions are the PB domains that were degraded and removed by ozonation, and the darker background is the PS matrix. (**B**) Hexagonally ordered arrays of holes in silicon nitride after RIE. The pattern was transferred from a copolymer film such as that in (A). The lighter regions are ~15-nm-deep holes that were etched out. (**C**) A cylindrical microdomain monolayer film before RIE. The darker lines are osmium-stained PB cylinders that lie parallel to the surface. (**D**) Fingerprintlike lines in silicon nitride after RIE. The pattern was transferred from a copolymer film such as that in (C). The darker regions are ~15-nm-thick ridges in the silicon nitride, which were protected from RIE.

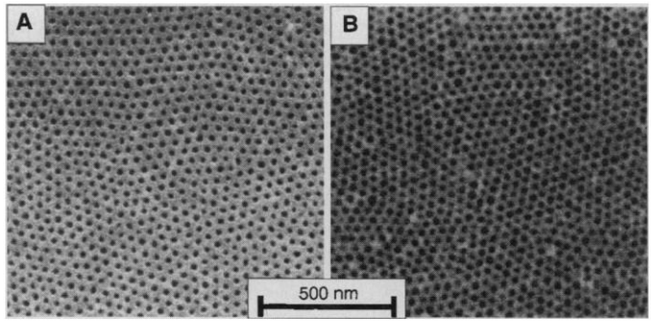

Fig. 3. (**A**) An SEM micrograph of a partially etched, ozonated monolayer film of spherical microdomains. After the continuous PS matrix at top was taken off (see Fig. 1B), the empty PI domains were exposed (as holes) and appear darker in the micrograph. (**B**) An SEM micrograph of hexagonally ordered arrays of holes in silicon nitride on a thick silicon wafer. The pattern was transferred from a copolymer film such as that in (A). The darker regions are ~20-nm-deep holes in silicon nitride, which have been etched out.

REFERENCES AND NOTES

1. H. Masuda and K. Fukuda, *Science* **268**, 1466 (1995); R. Gupta, J. J. McClelland, Z. J. Jabbour, R. J. Celotta, *Appl. Phys. Lett.* **67**, 1378 (1995); M. J. Lercel *et al.*, *J. Vac. Sci. Technol. B* **13**, 1139 (1995); M. Wendel, S. Kuhn, H. Lorenz, J. P. Kotthaus, M. Holland, *Appl. Phys. Lett.* **65**, 1775 (1994); M. A. McCord and D. D. Awschalom, *ibid.* **57**, 2153 (1990); H. Fang, R. Zeller, P. J. Stiles, *ibid.* **55**, 1433 (1989).
2. G. M. Whitesides, J. P. Mathias, C. T. Seto, *Science* **254**, 1312 (1991).
3. D. Hofstadter, *Phys. Rev. B* **14**, 2239 (1976); D. J. Thouless, M. Kohmoto, M. P. Nightingale, M. den Nijs, *Phys. Rev. Lett.* **49**, 405 (1982).
4. D. Weiss *et al.*, *Phys. Rev. Lett.* **66**, 2790 (1991).
5. W. Kang, H. L. Stormer, L. N. Pfeiffer, K. W. Baldwin, K. W. West, *ibid.* **71**, 3850 (1993).
6. W. D. Volkmuth and R. H. Austin, *Nature* **358**, 600 (1992); W. D. Volkmuth, T. Duke, M. C. Wu, R. H. Austin, A. Szabo, *Phys. Rev. Lett.* **72**, 2117 (1994).
7. S. Y. Chou, M. S. Wei, P. R. Krauss, P. B. Fischer, *J. Appl. Phys.* **76**, 6673 (1994).
8. T. L. Morkved *et al.*, *Science* **273**, 931 (1996).
9. T. L. Morkved, P. Wiltzius, H. M. Jaeger, D. G. Grier, T. A. Witten, *Appl. Phys. Lett.* **64**, 422 (1994).
10. P. Mansky, C. K. Harrison, P. M. Chaikin, R. A. Register, N. Yao, *ibid.* **68**, 2586 (1996); P. Mansky, P. Chaikin, E. L. Thomas, *J. Mater. Sci.* **30**, 1987 (1995).
11. Z. Li *et al.*, *J. Am. Chem. Soc.* **118**, 10,892 (1996).
12. F. S. Bates, *Science* **251**, 898 (1991); _____ and G. H. Fredrickson, *Annu. Rev. Phys. Chem.* **41**, 525 (1990).
13. The underlying silicon nitride layer is grown by a plasma-enhanced chemical vapor deposition technique. See S. M. Sze, *VLSI Technology* (McGraw-Hill, New York, ed. 2, 1988), pp. 233–271.
14. M. Park *et al.*, in *Symposium Proceedings*, vol. 461, *Morphological Control in Multiphase Polymer Mixtures*, Materials Research Society (MRS), Boston, 2 to 6 December 1996 (MRS, Pittsburgh, PA, 1997), pp. 179–184.
15. Because of the discrete microdomain size produced by self-assembly, spin-coated copolymer films on hard substrates rearrange into discrete film thicknesses upon annealing, which typically results in a nonuniform topography [see G. Coulon, D. Ausserre, T. P. Russell, *J. Phys. France* **51**, 777 (1990)]. However, by spin-coating initially at these discrete thicknesses, a uniform film can be produced even after annealing.
16. S. M. Sze, *VLSI Technology* (McGraw-Hill, New York, ed. 2, 1988), pp. 184–232.
17. The RIE parameters used here are CF_4 (100%), 2 mtorr, 10 standard cubic centimeters per minute (SCCM), 24 W, and ~290 V_{DC} [DC self-bias voltage of cathode (sample holder) with respect to plasma] and also CF_4/O_2 (90/10%), 25 mtorr, 20 SCCM, 20 W, and ~170 V_{DC}.
18. We obtained the TEM micrographs by spin-coating the copolymer films on thin (~75 nm) silicon nitride windows (50 μm by 50 μm) (Fig. 2). In this way, one can easily image the microdomain morphologies with the substrate intact before RIE and later directly view the patterned silicon nitride after RIE. The high-resolution TEM assists in characterizing and tuning the processing steps. Silicon nitride windows have been previously used in TEM micrography [see (*8*)]. Having a resolution and contrast of the image but not significantly at the 10-nm length scale.
19. The spherical microdomain monolayer shown in Fig. 2A is produced from SB 36/11, which exhibits a cylindrical morphology in bulk. A change from a cylindrical to a spherical morphology in thin films with a few nanometers of variation in film thickness has been observed and discussed previously (*14*).
20. The depth (or height) of the patterned structures is estimated from the etching times and rates (Figs. 2 and 3). In the case of the patterned silicon nitride layer on a silicon substrate in Fig. 3, the estimated number was confirmed by SEM on the cross section of a cracked sample.
21. In the case of the osmium-stained copolymer films (Fig. 1C), the addition of O_2 to CF_4 is necessary to obtain an etching selectivity between the PB and PS domains. However, in the case of the ozonated copolymer films (Fig. 1B), a pattern transfer to silicon nitride can be achieved whether pure CF_4 or CF_4/O_2 is used.
22. We observed that the discreteness of the microdomain monolayer thickness was less apparent for SI 68/12 when compared with SB 36/11. Even at thicknesses below 70 nm, we observed spherical PI microdomains over the entire sample area but with a poorer order.
23. C. Harrison *et al.*, in preparation.
24. We have produced a uniform microdomain monolayer template by spin-coating over an entire 76-mm wafer. With a larger ozonator system, the entire wafer would be patterned with the ordered nanostructure arrays.

25. We thank P. Mansky for helpful discussions. This project was supported by NSF through the Princeton Center for Complex Materials under grant DMR 9400362. Parts of the processing were carried out at the Advanced Technology Center for Photonics and Optoelectronic Materials at Princeton University and at the Cornell Nanofabrication Center. The silicon nitride windows were fabricated at the Cornell Nanofabrication Center.

3 February 1997; accepted 16 April 1997

Control of Mouse Cardiac Morphogenesis and Myogenesis by Transcription Factor MEF2C

Qing Lin, John Schwarz, Corazon Bucana, Eric N. Olson*

Members of the myocyte enhancer factor–2 (MEF2) family of MADS (MCM1, agamous, deficiens, serum response factor)–box transcription factors bind an A-T–rich DNA sequence associated with muscle-specific genes. The murine *MEF2C* gene is expressed in heart precursor cells before formation of the linear heart tube. In mice homozygous for a null mutation of *MEF2C*, the heart tube did not undergo looping morphogenesis, the future right ventricle did not form, and a subset of cardiac muscle genes was not expressed. The absence of the right ventricular region of the mutant heart correlated with down-regulation of the *dHAND* gene, which encodes a basic helix-loop-helix transcription factor required for cardiac morphogenesis. Thus, MEF2C is an essential regulator of cardiac myogenesis and right ventricular development.

The mechanisms that regulate heart formation during embryogenesis are only beginning to be elucidated (*1*). Members of the MEF2 family of transcription factors bind a conserved A-T–rich DNA sequence associated with most cardiac muscle structural genes (*2*) and are expressed in cardiogenic precursor cells and differentiated cardiomyocytes during embryogenesis (*3*). MEF2 factors are also expressed in skeletal and smooth muscle cell lineages (*3*, *4*), and MEF2 binding sites are essential for expression of muscle genes in all three muscle cell types (*5*).

There are four *MEF2* genes in vertebrate species, designated *MEF2A*, *-B*, *-C*, and *-D*, share homology in an NH_2-terminal MADS-box and an adjacent motif known as the MEF2 domain (*5*). These protein domains mediate DNA binding, homo- and heterodimerization, and interaction with basic helix-loop-helix (bHLH) transcription factors (*6–8*).

In the mouse, MEF2B and MEF2C are co-expressed in the precardiogenic mesoderm beginning at embryonic day 7.75 (E7.75), and MEF2A and MEF2D are expressed about 12 hours later (*3*, *8*). *MEF2* gene expression is detected in skeletal muscle precursors in the somites and in smooth muscle cells beginning at about E9.0. Loss-of-function mutations in a single *MEF2* gene in *Drosophila*, *D-mef2*, prevent differentiation of cardiac, skeletal, and visceral muscle cells (*9*), but the functions of the vertebrate *MEF2* genes in the embryo have not been determined.

To investigate *MEF2C* function during mouse embryogenesis, we inactivated this gene with a targeting vector (*10*) that deleted the second protein-coding exon, which encodes amino acids 18 to 86 (Fig. 1). The MADS and MEF2 domains are contained in residues 1 to 56 and 57 to 86, respectively, and the residues deleted by the mutation are essential for DNA binding and dimerization (*7*). The vector was introduced into embryonic stem (ES) cells by electroporation, clones were isolated after positive-negative selection (*11*), and genomic DNA was analyzed by Southern blot analysis for gene replacement at the *MEF2C* locus (*12*). The frequency of ES cell clones bearing a targeted *MEF2C* allele was 1:7. Three targeted ES cell clones were injected into blastocysts isolated from C57BL/6J mice to generate chimeras,

Q. Lin and E. N. Olson, Department of Molecular Biology and Oncology, University of Texas Southwestern Medical Center, 5323 Harry Hines Boulevard, Dallas, TX 75235–9148, USA.
J. Schwarz, Division of Cardiology, Department of Internal Medicine, University of Texas Medical School, Houston, TX 77030, USA.
C. Bucana, Department of Cell Biology, University of Texas M. D. Anderson Cancer Center, Houston, TX 77030, USA.
*To whom correspondence should be addressed.